Sanjeeva Balasuriya, Benjamin J. Binder
Nonautonomous analysis of steady Korteweg-de Vries waves under nonlocalised forcing
Physica D: Nonlinear Phenomena, 2014; 285:28-41

Final publication at http://dx.doi.org/10.1016/j.physd.2014.07.001

Nonautonomous analysis of steady Korteweg-de Vries waves under nonlocalised forcing

Sanjeeva Balasuriya[a], Benjamin J. Binder[a]

[a] *School of Mathematical Sciences, University of Adelaide, Adelaide SA 5005, Australia*

Abstract

Recently developed nonautonomous dynamical systems theory is applied to quantify the effect of bottom topography variation on steady surface waves governed by the Korteweg-de Vries (KdV) equation. Arbitrary (but small) nonlocalised bottom topographies are amenable to this method. Two classes of free surface solutions— hyperbolic and homoclinic solutions of the associated augmented dynamical system—are characterised. The first of these corresponds to near-uniform free-surface flows, and explicit formulæ are developed for a range of topographies. The second corresponds to solitary waves on the free surface, and a method for determining their number is developed. Formulæ for the shape of these solitary waves are also obtained. Theoretical free-surface profiles are verified using numerical KdV solutions, and excellent agreement is obtained.

Keywords: nonautonomous dynamical systems, homoclinic trajectories, KdV equation, free-surface flow, solitary waves

1. Introduction

The Korteweg-de Vries (KdV) equation is an archetypical evolution equation representing the balance of dispersion and weak nonlinearity in physical systems that generate waves. The physical motivation behind the original derivation of Korteweg and de Vries [1] was to describe long waves propagating in a rectangular channel, but there are also applications in ion acoustic waves in a plasma, acoustic waves on a crystal lattice, and coupled oscillators [2, 3, 4, 5, 6]. The richness of the behaviour of solutions is such that there continues to be ongoing numerical and analytical studies to the KdV equation [7, 8, 9, 10, 11, 12, 13, cf.].

The form we examine in this article is the steady forced KdV equation represented in the dimensionless form [4, 5, 14, 15, 16, 17, 11, 18]

$$\eta_{xxx} + 9\eta\eta_x - 6\,(F-1)\,\eta_x = -3p_x\,. \tag{1}$$

The equation approximates the elevation $\eta(x)$ of the interface between the water and air (free-surface) in a two-dimensional (x, y) gravity affected channel flow. The flow can be characterised with the dimensionless Froude number

$F = U/\sqrt{gH}$, where U and H are the uniform flow speed and depth in the far field, and g is the acceleration due to gravity. We focus here specifically on the role of the forcing term $p(x)$, which represents either bottom topography, or an external surface pressure on the free-surface. The existence of a solitary wave solution is well-established for $p \equiv 0$ [1, 19]; in this article, we find analytical approximations for solitary waves and allied solutions when $p \neq 0$, but is small.

When there is no forcing (i.e., with $p \equiv 0$), (1) is autonomous, and is well-understood in terms of the autonomous (η, η_x) phase plane (Fig. 1(b)). An analysis for determining free-surface solutions can be performed in the *same* autonomous phase plane when p takes on very specific forms. In the case of Dirac delta forcing (corresponding to a localised forcing or bump in bottom topography), solutions can be rationalised as jumping from one solution trajectory to another in the autonomous phase space [5, 16, 17, 20]. A jump also results from the presence of an inclined plane on the surface [21]. If p represents a vertical step at the bottom, solutions can be formed through the intersection of solution trajectories belonging to two different autonomous phase spaces [22, 23]. Combinations of these three types of forcing (bump, plate and step) have also been studied in a similar way for hybrid flows with multiple disturbances [23, 24, 25, 26], with an obvious limitation to a more general type of nonlocalised forcing.

A specific class of nonlocalised p has received some attention in the literature: sinusoidal functions. When the amplitude of the sinusoid is small, several studies have established the presence of chaos in the KdV and similar equations [27, 28, 29, 30, 31]. The main tool used in these analyses is the Melnikov function from dynamical systems theory [32, 33, 34], whose zeroes correspond to intersections between stable and unstable manifolds, and hence chaos via the Smale-Birkhoff theorem [33]. These studies do not focus on obtaining free-surface profiles theoretically, since the classical Melnikov function does not by itself relate to such profiles. However, recent theoretical developments [35, 36] building on the Melnikov approach provide the proper framework for determining free-surface profiles for *general* $p(x)$, under the sole condition that p is small; indeed, Dirac delta forms are also permissible [37]. The key tool developed by Balasuriya [35] quantifies the normal and tangential motion of a stable and/or unstable manifold due to the presence of a nonautonomous perturbation. In this article, we adapt this theory to enable quantification of the free-surface profile for the KdV equation for any small p.

In obtaining the free-surface profiles for general p, we need to view the KdV system not in the (η, η_x)-phase space as is standard for autonomous or "jumping between autonomous" situations [5, 20, 16, 17, 21, 22, 23, 24, 25, 26], but in the genuinely nonautonomous (η, η_x, x) phase space. This standard approach from dynamical systems is apparently not present in the KdV literature, and is described in Section 2. This framework enables us to develop two classes of free-surface solutions which we classify according to dynamical systems terminology as *hyperbolic* trajectories and *homoclinic* solutions. These solution classes correspond respectively to near-uniform and near-solitary wave solutions of the KdV equation, analogous to the perturbation of a uniform stream and perturbation

of a solitary wave classification of Vanden-Broeck [38]. In Section 3 we establish an analytical formula which approximates the hyperbolic (near-uniform) solution, proving moreover that for general p there is a unique hyperbolic solution. Physically, this means that there is one and only one near-uniform free-surface configuration for the steady forced KdV equation for small bottom topography. In Section 4 we establish a criterion for determining the number of homolinic (near-solitary) solutions for a given forcing function; here 'homoclinic' means that the solution lies on both the stable and the unstable manifold associated with the hyperbolic trajectory. This supplements theoretical results by Choi et al. [18] which characterises this number for compactly supported even p; here, we establish a tool which works for general p. We then adapt the theory of Balasuriya [35] to formulate an analytical formula which approximates each of these near-solitary waves. In Section 5, we demonstrate the excellent agreement between our theoretical formulæ and numerical solutions to the KdV equation, finding along the way several unusual looking steady solitary waves. Our ability to provide explicit analytical formulæ for the free-surface gives excellent initial guesses for our numerical KdV schemes. These can also be utilised as initial guesses in nonlinear free-surface computations beyond the weakly nonlinear (KdV) approximation [16, 17, 21, 22, 24, 25].

In this work we restrict our analysis to supercritical flow with $F > 1$. The technical reason for this restriction is that in this case, the physically relevant near-uniform free-surface configuration which corresponds to $(\eta, \eta_x) = (0, 0)$, is a saddle point in the phase plane of Fig. 1(b). Such points—or more precisely their nonautonomous analogues— are structurally stable. Thus, when p is small but nonzero, a similar near-uniform solution persists; this is our hyperbolic trajectory. Moreover, the stable and unstable manifolds persist, allowing for the possibility of them intersecting to create a homoclinic solution which asymptotes to the hyperbolic solution as $x \to \pm\infty$. If we considered subcritical flow in which $F < 1$, the phase-portrait of Fig. 1(b) changes somewhat; a centre (elliptic) point now lies at the uniform free-surface location $(\eta, \eta_x) = (0, 0)$ [16]. Such an entity is not structurally stable, and thus its persistence cannot be guaranteed for p small but nonzero. Thus, our analysis for determining near-uniform or near-solitary solutions breaks down for $F < 1$. The critical case of $F = 1$, addressed in [39], is also not amenable to the present analysis since once again structural stability of the near-uniform solution is not assured.

2. Nonautonomous viewpoint

As our governing equation, we consider the integrated version of (1) given by

$$\eta_{xx} + \frac{9}{2}\eta^2 - 6\,(F-1)\,\eta = -3p(x) \tag{2}$$

in the supercritical regime $F > 1$, where following many authors [1, 23, 28, 40] we have set the integration constant to zero to deal with a class of bounded solutions of (1). We remark that an equation equivalent to (2) would also result

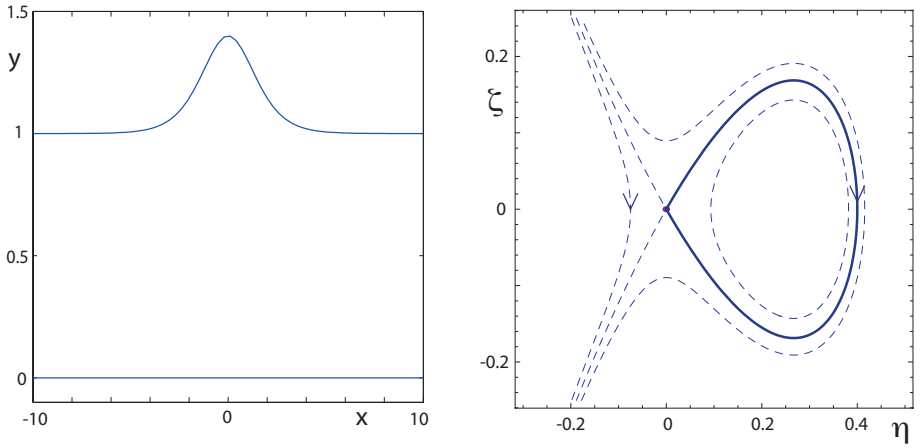

Figure 1: Unforced solitary wave, with $y = \eta + 1$, $p(x) \equiv 0$ and $F = 1.2$. (a) Free-surface profile. (b) Autonomous phase space $\zeta = \eta_x = \eta'$ versus η.

if considering travelling wave solutions to the *unsteady* KdV equation in which there were a surface forcing which also travels with the wave [12, 28, 30, 40]; our analysis is also applicable for determining travelling wave profiles in that instance. We impose the smallness condition

$$|p(x)| \leq |\varepsilon| \ll F - 1 \tag{3}$$

for all $x \in \mathbb{R}$ on the forcing function p. Upon defining the variable $\zeta = \eta'(x)$, (2) can be written as

$$\left.\begin{aligned} \eta' &= \zeta \\ \zeta' &= -\frac{9}{2}\eta^2 + 6(F-1)\eta - 3p(x) \end{aligned}\right\}, \tag{4}$$

which is *nonautonomous* because p depends explicitly on the independent variable x. Thus, (4) may be best viewed in the (η, ζ, x) appended (or augmented) space as

$$\left.\begin{aligned} \eta' &= \zeta \\ \zeta' &= -\frac{9}{2}\eta^2 + 6(F-1)\eta - 3p(x) \\ x' &= 1 \end{aligned}\right\}. \tag{5}$$

In this section, we describe the well-known situation $p \equiv 0$ within the setting of (5), to enable us to investigate $p \neq 0$ subsequently. When $p \equiv 0$, there are two well-known special solutions to (4), of which the first is the trivial solution $(\eta, \zeta) = (0, 0)$, corresponding to a flat surface with no additional features. We shall also refer to this as the uniform stream solution. The linearised matrix of (4) around this zero solution has eigenvalues $\pm\sqrt{6(F-1)}$, implying $(0, 0)$ is a saddle fixed point possessing one-dimensional stable and unstable manifolds, in

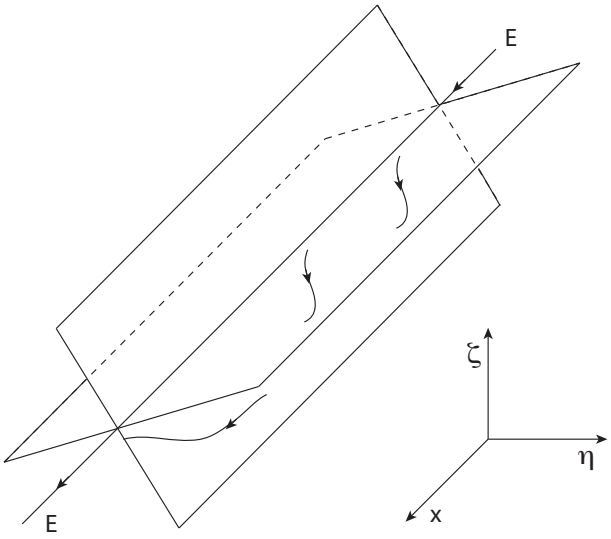

Figure 2: A local picture of the hyperbolic trajectory **E** (heavy arrow) given by (6) in the augmented phase space, with its attached stable and unstable manifolds also shown.

the autonomous phase portrait as shown in Fig. 1(b). Now, this zero solution when viewed in the augmented phase space (η, ζ, x) of (5) is

$$\mathbf{E}(x) = \begin{pmatrix} \eta \\ \zeta \\ x \end{pmatrix}(x) = \begin{pmatrix} 0 \\ 0 \\ x \end{pmatrix}, \tag{6}$$

which forms a trajectory along the x-axis. This trajectory is *hyperbolic* since it possesses both a two-dimensional stable manifold and a two-dimensional unstable manifold, corresponding to the one-dimensional entities associated with viewing this solution in the autonomous phase space (4). These manifolds are foliated with trajectories which forwards or backwards asymptote to the hyperbolic trajectory (6), as shown in Fig. 2.

The second special solution to (4) when $p \equiv 0$ is the one-parameter family of solutions $(\eta, \zeta) = (\bar{\eta}_\alpha(x), \bar{\eta}'_\alpha(x))$ where

$$\bar{\eta}_\alpha(x) = 2\,(F-1)\,\mathrm{sech}^{\,2}\left(\sqrt{\frac{3(F-1)}{2}}\,[x-\alpha]\right), \tag{7}$$

with α being an arbitrary parameter. The profile (7) is the familiar solitary wave [1] as shown in Fig.1(a), which is a solution for any α since the solitary wave can be centred at any location. In terms of the fundamental solitary wave solution

$$\bar{\eta}(x) = 2\,(F-1)\,\mathrm{sech}^{\,2}\left(\sqrt{\frac{3(F-1)}{2}}\,x\right), \tag{8}$$

the family (7) can be represented as shifts defined by $\bar{\eta}_\alpha(x) = \bar{\eta}(x-\alpha)$. Each $\bar{\eta}_\alpha$ corresponds to a connection from the saddle point to itself, represented by the bold curve in Fig. 1(b). By choosing any point on this segment as an initial condition, the solution will forward asymptote to the fixed point at the origin, and will backwards asymptote to the *same* fixed point. Thus, this solution corresponds to a homoclinic trajectory of the fixed point $(0,0)$, since it is simultaneously part of its stable and unstable manifold. The freedom to choose any point as an initial condition is exactly the freedom of choosing α in (7); if for example $(\eta,\zeta) = (2(F-1),0)$ were chosen, this corresponds to choosing the symmetric solution $\alpha = 0$ in (7), i.e., to choosing (8).

With respect to the augmented phase space (η,ζ,x), this family of solutions (7) take the form

$$\mathbf{N}_\alpha(x) = \begin{pmatrix} \bar{\eta}_\alpha(x) \\ \bar{\eta}'_\alpha(x) \\ x \end{pmatrix} . \tag{9}$$

Since $\bar{\eta}_\alpha(x)$ asymptotes to zero in both the limits $x \to \pm\infty$, each $\mathbf{N}_\alpha(x)$ lies on both the stable and the unstable manifold of the hyperbolic trajectory $\mathbf{E}(x)$ as given in (6), in the augmented phase space. Thus the solutions $\mathbf{N}_\alpha(x)$ all lie on the homoclinic manifold of $\mathbf{E}$, and shall be called *homoclinic solutions*. These exhibit the behaviour

$$\lim_{x\to\pm\infty} |\mathbf{N}_\alpha(x) - \mathbf{E}(x)| = 0\,,$$

for all $\alpha \in \mathbb{R}$, implying that when $p = 0$ in (5), there are infinitely many homoclinic solutions. From the perspective of Fig. 2, a branch of each of the stable and unstable manifolds shown in the local picture near the hyperbolic trajectory $\mathbf{E}$ in Fig. 2 connect up; this is the augmented phase space visualisation of the closed homoclinic manifold shown in Fig. 1. The geometric structure of this homoclinic manifold in the augmented phase space is shown in Fig. 3. The manifold is foliated with trajectories $\mathbf{N}_\alpha(x)$ which backwards and forwards asymptote to $\mathbf{E}$. The parameter α represents which particular trajectory on the manifold is chosen. The ability to "slide" the solitary wave to any location (centred at $x = \alpha$) when thinking of η as a function of x, corresponds exactly to choosing a particular trajectory selected by α.

Now when the imposed forcing $p(x)$ is included, (4) becomes genuinely nonautonomous, and here the augmented phase space representation (5), along with the geometry we have described, becomes invaluable. We will show that the hyperbolic solution perturbs to a nearby solution, while the family of homoclinic solutions may perturb to nearby solutions based on a criterion which we identify. Moreover, we will determine explicit analytical expressions for all these solutions for any general $p(x)$.

3. Hyperbolic solutions

In this section, we consider the associated perturbation to the hyperbolic solution $\mathbf{E}$ as given in (6). *Only* the smallness of p as expressed in (3) is needed

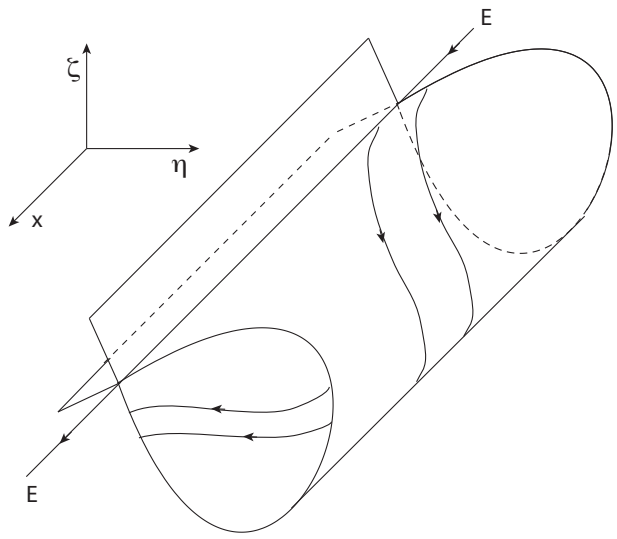

Figure 3: The homoclinic manifold of $\mathbf{E}$ in the augmented phase space, which is foliated by the the homoclinic solutions $\mathbf{N}_\alpha$ (two of which are shown) as given in (9).

for our analysis; we do not require restrictions such as p being localised or compactly supported [5, 20, 16, 17, 18, 41, e.g.], going to zero in the limits $x \to \pm\infty$ [5, 20, 16, 17, 21, 22, 23, 24, 25, 26, e.g.], being spatially periodic [27, 28, 29, 30, 31, e.g.], or being smoothly differentiable. For small enough $|\varepsilon|$, there are theoretical results [42, 43, 44] which ensure that there exists a trajectory

$$\mathbf{E}^\varepsilon(x) = \begin{pmatrix} \eta^\varepsilon(x) \\ \zeta^\varepsilon(x) \\ x \end{pmatrix} = \begin{pmatrix} \eta^\varepsilon(x) \\ (\eta^\varepsilon)'(x) \\ x \end{pmatrix} \tag{10}$$

of (5) such that $|\mathbf{E}^\varepsilon(x) - \mathbf{E}(x)| \leq C\,|\varepsilon|$ for some constant C independent of x, and moreover $\mathbf{E}^\varepsilon(x)$ is hyperbolic. Defining hyperbolicity in this nonautonomous context requires an understanding of exponential dichotomies [42, 45, 46] but the basic intuition is easily stated: the exponential decay rates associated with the stable and unstable manifolds of $\mathbf{E}$ are preserved to leading-order in ε for a trajectory nearby $\mathbf{E}$. This trajectory, given in (10), thus itself possesses two-dimensional stable and unstable manifolds (which are associated with the exponential decay rates), rendering the behaviour near $\mathbf{E}^\varepsilon$ topologically identical to that near $\mathbf{E}$. In other words, the new picture for $p \neq 0$ is simply a wobbled version of Fig. 2. The closeness to $\mathbf{E}$ means that the free surface flow remains $\mathcal{O}(\varepsilon)$-close to a flat surface, and so (10) is a "near-uniform flow" solution. We remark that in making this argument, we needed to have the uniform solution $(0,0)$ to be hyperbolic, which is the reason for our restricting our attention to $F > 1$. If $F < 1$, the point $(0,0)$ is elliptic (a centre) [16], and its nearby structure cannot be guaranteed to persist under perturbations.

Determining a leading-order expression for the hyperbolic trajectory (10), and thus the small amplitude wave on the surface, can be done using a theoretical development valid in this nonautonomous case, using the approach of Balasuriya [35]. The formula for the η-term in $\mathbf{E}^\varepsilon$ turns out to be

$$\eta^\varepsilon(x) = \frac{3}{2\sqrt{6(F-1)}} \int_0^\infty \left[p(x-\tau) + p(x+\tau)\right] e^{-\sqrt{6(F-1)}\tau}\, \mathrm{d}\tau + \mathcal{O}(\varepsilon^2)\,. \quad (11)$$

The derivation of this surprisingly simple formula is given in Appendix A, along with the proof of the *existence and uniqueness* of this particular trajectory which is $\mathcal{O}(\varepsilon)$-close to the uniform stream (i.e., flat free surface). In other words, the nonautonomous technique that we use establishes that there is one and only one free surface configuration for a given $\mathcal{O}(\varepsilon)$ form of p, which has size $\mathcal{O}(\varepsilon)$ uniformly for all $x \in \mathbb{R}$. Thus, it is a pointless exercise to seek additional such solutions numerically or otherwise. In Section 5, we shall provide explicit near-uniform free-surface profiles using (11).

An interesting point regarding (11) is that a quick method for attempting to derive it would be to neglect the nonlinear term $(9/2)\eta^2$ in (2), and then use variation of parameters on the linear system. The leading-order term in (11) does indeed take the form of such a variation of parameters solution, providing an additional check on the solution (11). However, such a variation of parameters approach by itself fails in identifying the hyperbolic trajectory (11), since there is no *a priori* way to know what particular "initial" conditions to apply at $x = 0$. Conditions at $\pm\infty$ are also not available, since p need not decay in these limits. Moreover, a variation of parameters approach would not guarantee hyperbolicity, or rigorously ensure that the remaining terms in (11) are $\mathcal{O}(\varepsilon^2)$. Thus the approach of Appendix A—which deals with all these issues—is necessary in deriving the hyperbolic solution.

4. Homoclinic solutions

Since the persistent trajectory $\mathbf{E}^\varepsilon$ is hyperbolic in the sense of exponential dichotomies, in the augmented phase space it continues to possess two-dimensional stable and unstable manifolds. When p was zero, a branch of each of these coincided to form the homoclinic manifold foliated by the solitary wave solutions $\mathbf{N}_\alpha$ as shown in Fig. 3. However, when $p \neq 0$, these two branches of manifolds are *not* guaranteed to coincide. But if they do intersect, such points would lie on both the stable and unstable manifolds of $\mathbf{E}^\varepsilon$, and thereby be associated with a homoclinic solution.

Generically, two-dimensional surfaces will intersect along curves. Any point on an intersection curve, since it is on the stable manifold of $\mathbf{E}^\varepsilon$, must backwards asymptote to $\mathbf{E}^\varepsilon$ under the flow of (5). At the same time, since it is also on the unstable manifold of $\mathbf{E}^\varepsilon$, it must also forward asymptote to $\mathbf{E}^\varepsilon$. In doing so, it must pass through points which continue to lie on both manifolds; this trajectory of (5) is therefore *the* intersection curve we seek, and corresponds to a homoclinic trajectory of $\mathbf{E}^\varepsilon$. There may be zero, one, finitely many, or

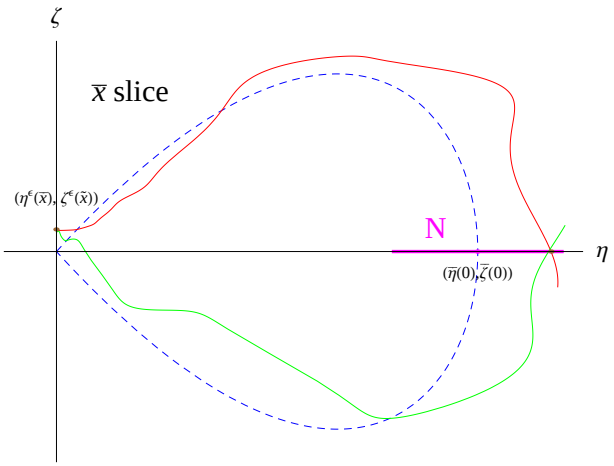

Figure 4: The perturbed stable and unstable manifolds in the spatial slice $\bar{x}$, in which they intersect along the normal line N to the original homoclinic.

even infinitely many such intersection curves, comprising the set of *homoclinic solutions*.

Since visualising this geometry in three dimensions is difficult, we will explain these intersections in terms of x-slices of the augmented phase space. We define

$$M(x) := \int_{-\infty}^{\infty} \operatorname{sech}^2\left(\sqrt{\frac{3(F-1)}{2}}\tau\right) \tanh\left(\sqrt{\frac{3(F-1)}{2}}\tau\right) p(x+\tau)\,\mathrm{d}\tau\,. \qquad (12)$$

The function $M(x)$ represents the leading-order scaled displacement in the spatial slice x, between the stable and unstable manifolds when measured along the normal line N to the original homoclinic drawn at the point $(\bar{\eta}(0), \bar{\eta}'(0))$, which is the point $(2(F-1), 0)$. This interpretation justifies us calling M a *Melnikov function* [33, 34, 47]. An illustration of this is shown in Figs. 4 and 5. In Fig. 4 the manifolds intersect along N, and thus at this special x-value, which we shall call $\bar{x}$, $M(\bar{x}) = 0$. A general x-value is shown in Fig. 5, and in this case $M(x)$ is nonzero. This description of M as quantifying intersections along N can be theoretically justified [33, 35]; Appendix B shows that if there exists a $\bar{x} \in \mathbb{R}$ satisfying

$$M(\bar{x}) = 0 \quad \text{and} \quad M(\bar{x}) \text{ crosses zero at } \bar{x}\,, \qquad (13)$$

then there exists a homoclinic solution which is $\mathcal{O}(\varepsilon)$-close to an autonomous homoclinic trajectory. Conversely, if M has no zeroes, then for small enough $|\varepsilon|$ there are no $\mathcal{O}(\varepsilon)$-close homoclinic trajectories. Thus, (13) provides an easily checkable condition for the checking the existence of solitary waves which are $\mathcal{O}(\varepsilon)$-close to an $\mathbf{N}_\alpha$.

If (13) is satisfied, there exists an intersection of stable and unstable manifolds at an x-value which is $\mathcal{O}(\varepsilon)$-close to $\bar{x}$, since $M(x)$ represents only the

leading-order distance as shown in Fig. 5. A homoclinic solution can then be determined by matching together trajectories lying on the stable and unstable manifolds at $x = \bar{x}$. As explained in detail in Appendix B, the theoretical development by Balasuriya [35] can be adapted to obtain that the corresponding homoclinic solution has the form

$$\eta^{\varepsilon}_{\bar{x}}(x) = \bar{\eta}(x-\bar{x}) + [\eta^{\varepsilon}_n(x) + \eta^{\varepsilon}_t(x)] + \mathcal{O}(\varepsilon^2) \tag{14}$$

in which $\bar{\eta}$ is the fundamental solitary wave solution (8), and η^{ε}_n and η^{ε}_t are respectively the *n*ormal and *t*angential $\mathcal{O}(\varepsilon)$-corrections to the wave, given by

$$\eta^{\varepsilon}_n(x) = \begin{cases} \dfrac{3\bar{\eta}''(x-\bar{x})}{\bar{\eta}'(x-\bar{x})^2 + \bar{\eta}''(x-\bar{x})^2} \displaystyle\int_{-\infty}^{x-\bar{x}} \bar{\eta}'(\tau) p(\tau+\bar{x})\,\mathrm{d}\tau & \text{if } x \le \bar{x} \\ -\dfrac{3\bar{\eta}''(x-\bar{x})}{\bar{\eta}'(x-\bar{x})^2 + \bar{\eta}''(x-\bar{x})^2} \displaystyle\int_{x-\bar{x}}^{\infty} \bar{\eta}'(\tau) p(\tau+\bar{x})\,\mathrm{d}\tau & \text{if } x > \bar{x} \end{cases}, \tag{15}$$

and

$$\frac{\eta^{\varepsilon}_t(x)}{-3\bar{\eta}'(x-\bar{x})} = \begin{cases} \displaystyle\int_0^{x-\bar{x}} \frac{\bar{\eta}''(\tau)p(\tau+\bar{x}) + \Omega(\tau)\int_{-\infty}^{x-\bar{x}} \bar{\eta}'(\lambda)p\left(\lambda+\tau-x+2\bar{x}\right)\,\mathrm{d}\lambda}{\bar{\eta}'(\tau)^2 + \bar{\eta}''(\tau)^2}\,\mathrm{d}\tau & \text{if } x \le \bar{x} \\ \displaystyle\int_0^{x-\bar{x}} \frac{\bar{\eta}''(\tau)p(\tau+\bar{x}) - \Omega(\tau)\int_{x-\bar{x}}^{\infty} \bar{\eta}'(\lambda)p\left(\lambda+\tau-x+2\bar{x}\right)\,\mathrm{d}\lambda}{\bar{\eta}'(\tau)^2 + \bar{\eta}''(\tau)^2}\,\mathrm{d}\tau & \text{if } x > \bar{x} \end{cases} \tag{16}$$

where

$$\Omega(\tau) := \frac{\left[6F - 9\bar{\eta}(\tau) - 5\right]\left[\bar{\eta}'(\tau)^2 - \bar{\eta}''(\tau)^2\right]}{\bar{\eta}'(\tau)^2 + \bar{\eta}''(\tau)^2}\,. \tag{17}$$

The reason for this terminology is based on phase space geometry, as we shall explain. In the spatial slice $\bar{x}$, the intersection between the stable and the unstable manifold lies on the normal N drawn to the unperturbed homoclinic at $(\bar{\eta}(0), \bar{\eta}'(0))$ as shown in Fig. 4. Since we now want its location in a general spatial slice x, the corresponding unperturbed homoclinic trajectory we must consider is $\bar{\eta}(x-\bar{x})$, since this when evaluated at $x = \bar{x}$ gives $\bar{\eta}(0)$, the location at which the N was drawn. Any existing nearby homoclinic connection thus must remain close to $\bar{\eta}(x-\bar{x})$, as indicated in (14).

In a general slice x, the intersection point evolves to a location which is $\mathcal{O}(\varepsilon)$-close to $(\bar{\eta}(x-\bar{x}), \bar{\eta}'(x-\bar{x}))$, as shown in Fig. 5. (We note that the stable/unstable manifolds are in general different entities than in Fig. 4, reflecting their nonautonomous nature.) The intersection point corresponds to the homoclinic trajectory, since it is the x-evolved location of the intersection point which was located on the normal line in the spatial slice $\bar{x}$ as shown in Fig. 4. This point need not lie on the normal N_x drawn at the point $(\bar{\eta}(x-\bar{x}), \bar{\eta}'(x-\bar{x}))$. The vector $\mathbf{v}$ drawn from $(\bar{\eta}(x-\bar{x}), \bar{\eta}'(x-\bar{x}))$ to this intersection point (pictured by the small arrow in Fig. 5) can be split into a vector normal to the original homoclinic (that is, to a vector pointing along N_x) which shall be called $\mathbf{v}_n$, plus a vector tangential to the unperturbed homoclinic called $\mathbf{v}_t$. The relevance of

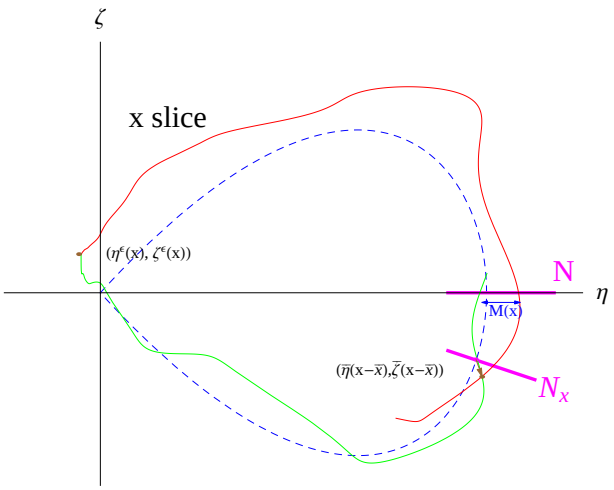

Figure 5: The positioning of the perturbed stable and unstable manifolds in a general spatial slice x, illustrating the intuitive meaning of $M(x)$ in (12), and the representation of the homoclinic point vectorially from the point $(\bar{\eta}(x-\bar{x}), \bar{\eta}'(x-\bar{x}))$.

such a tangential component $\mathbf{v}_t$ has only recently been recognised, and characterised to leading-order [35]; classical Melnikov approaches [33, 34] are limited to quantifying the normal separation, which is also relevant to quantifying and optimising transport [48, 37, 49, 50, 51, 52]. As we shall show numerically, ignoring the tangential component leads to results which are substantially incorrect in this particular situation, highlighting the importance of the development by Balasuriya [35]. Now, in determining the homoclinic solution, we are principally interested only in the η-component (the $\zeta = \eta'$ component is simply the x-derivative of this), and thus we only need the η-component of each of $\mathbf{v}_n$ and $\mathbf{v}_t$. The η-component of $\mathbf{v}_n$, since it is associated with the normal correction, is what is called η_n^ε in (14). Similarly, the η-component of $\mathbf{v}_t$, being related to the tangential correction, is called η_t^ε.

The homoclinic solution (14) is $\mathcal{O}(\varepsilon)$-close (for all $x \in \mathbb{R}$) to an unperturbed homoclinic solution $\mathbf{N}_{\bar{x}}$, i.e., its leading-order term corresponds to choosing $\alpha = \bar{x}$ in (7). Moreover, (14) is a *nonautonomous* solitary wave since its front end ($x \to \infty$) need not decay to a constant, but will remain $\mathcal{O}(\varepsilon)$-close to 0. The same is true in the limit $x \to -\infty$. Since the solution (14) lies on both the stable and unstable manifold of $\mathbf{E}^\varepsilon$, it obeys as

$$\lim_{x \to \pm\infty} |\eta_{\bar{x}}^\varepsilon(x) - \eta^\varepsilon(x)| = 0 \tag{18}$$

for all $\eta_{\bar{x}}^\varepsilon$ satisfying (14) and η^ε satisfying (11). Physically, this means that all solitary wave solutions must approach the unique near-uniform solution in the far field.

It must be emphasised that for every $\bar{x}$ satisfying (13), there is a correspond-

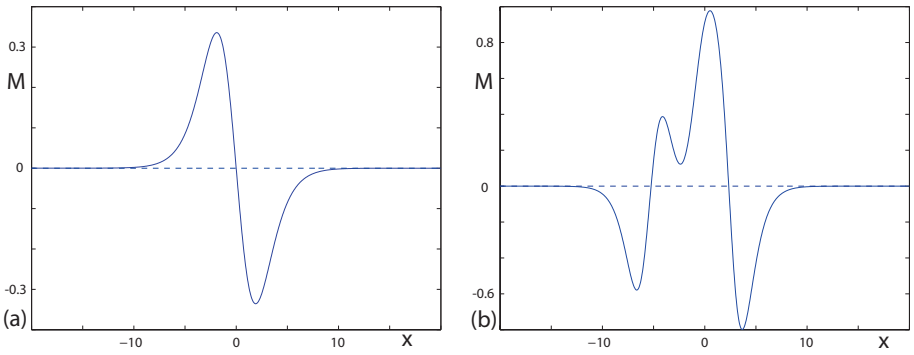

Figure 6: The Melnikov function $M(x)$ as given in (12), for (a) Gaussian topography (20) with $b = 1$ and $F = 1.1$, and (b) jagged topography (20) with $F = 1.2$.

ing solitary wave solution which has the behaviour described above. Thus, if (13) is satisfied for at least one $\bar{x}$, there will exist nonunique solutions which have the same decay characteristics as $x \to \pm\infty$; one solution which is the hyperbolic trajectory $\mathbf{E}^{\varepsilon}$, and another which is a homoclinic solution expressed by (14). Such nonuniqueness when $F = 1$ was explored numerically by Binder et al. [39]. Of course, there may be one, several, or even infinitely many, homoclinic solutions achievable depending on the number of solutions $\bar{x}$ to (13). It is also possible that there are *no* solutions to (13), in which case there will be no solitary wave solutions for small ε despite there being uncountably many when $\varepsilon = 0$. We remark that under evenness and sufficiently rapid decay at $\pm\infty$ for p, it is known that there is exactly one solution which satisfies evenness and exponential decay [53], but in general the number of near-solitary wave solutions depends on the nature of p, and can be determined using our approach of examining zeroes of $M(x)$ in (12).

5. Results

We benchmark our theory by considering Gaussian bottom topography [12, 15, 24, 54]

$$p(x) = \frac{\varepsilon b}{\sqrt{\pi}} e^{-b^2 x^2} \tag{19}$$

for some parameter b. Since p is even, $M(x)$ in (12) has a zero at $\bar{x} = 0$. A plot of the Melnikov function for $b = 1$ and $F = 1.1$ is shown in Fig. 6(a), indicating there are no other zeroes. Using (11) and (14), we can compute the theoretical hyperbolic (I) and homoclinic (II) solutions, and show them when $F = 1.1$, $b = 1$ and $\varepsilon = 0.02$ as the dashed curves in Fig. 7(a). The solid curves are solitary wave trajectories computed numerically from the KdV equation (2) using (19), indicating excellent agreement, with the maximum errors occurring near the centre point, at the point of greatest height of the waves. In Fig. 7(b), we investigate the maximum part of the error's dependence on ε, by plotting

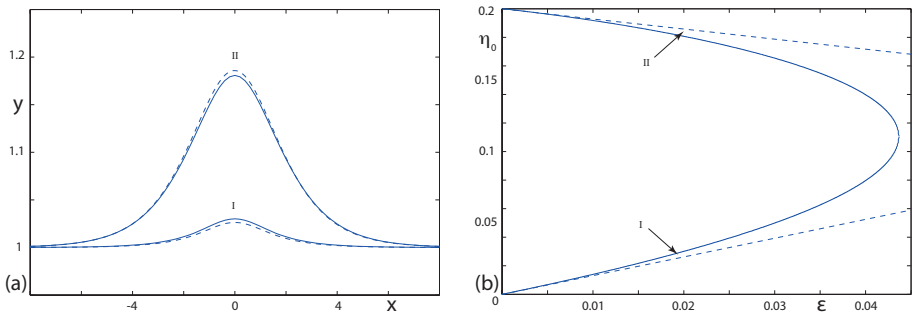

Figure 7: Comparison between theoretical (*dashed*) and numerical (*solid*) solutions for a Gaussian topography (19) with $F = 1.1$ and $b = 1$. (a) Free-surface profiles with $\varepsilon = 0.02$. (b) Plot of the free-surface elevation $\eta(0) = \eta_0$ versus ε. with the solutions in (a) indicated with arrows.

the height of the solitary waves obtained numerically (solid curve), along with the heights of the hyperbolic and homoclinic solutions computed theoretically (bottom and upper almost straight dashed lines). The hyperbolic and homoclinic solutions presented in Fig. 7 are respectively the perturbation of a uniform stream, and perturbation of a solitary wave, solutions of Vanden-Broeck [38], providing a further check on our analysis.

As a second example, we consider

$$\begin{aligned} p(x) \quad = \quad & \varepsilon\Big\{\operatorname{sech} x \tanh x - 5\left[\tanh\left(100(x-2)\right) - \tanh\left(100(x-3)\right)\right](x-2)\,(x-3) \\ & +0.4\left[\tanh\left(100(x+6)\right) - \tanh\left(100(x+4)\right)\right](x+4)\Big\}. \end{aligned} \tag{20}$$

This function has non-compact support, and has fairly jagged topography variations. In order to determine the number of solitary waves possible, we compute the Melnikov function M in (12), and show it in Fig. 6(b) for $F = 1.2$. The two zero crossings correspond to $\bar{x} = -5.2410$ and 2.3446; there are exactly two homoclinic solutions for small ε. The hyperbolic trajectory computed using (11) is shown in Fig. 8(a), and the two homoclinic solutions computed using (14) are shown in Figs. 8(b) and (c). Thus, there are at least *three* free-surface solutions associated with (20) for small ε; one near-uniform free-surface, and two solitary wave configurations. We contrast the theoretical homoclinic solutions with Fig. 8(d), in which we perform the computation of the two homoclinic trajectories incorrectly by neglecting the tangential term $\eta_{\bar{x}}^t$ in (14). Unlike the correct solutions in Figs. 8(b) and (c), the incorrectly computed solitary waves in Fig. 8(d) do not decay quickly towards the free-surface solution. This demonstrates the importance of the recently developed tangential correction [35]; without incorporating this correctly, false results are obtained.

In Fig. 9, we show direct numerical computations using the KdV equation (2), such that (a), (b) and (c) correspond exactly to the scenarios of Fig. 8. We used the theoretical solutions of Fig. 8 as initial values for our numerical computations, and obtained rapid convergence to the solutions. The agreement

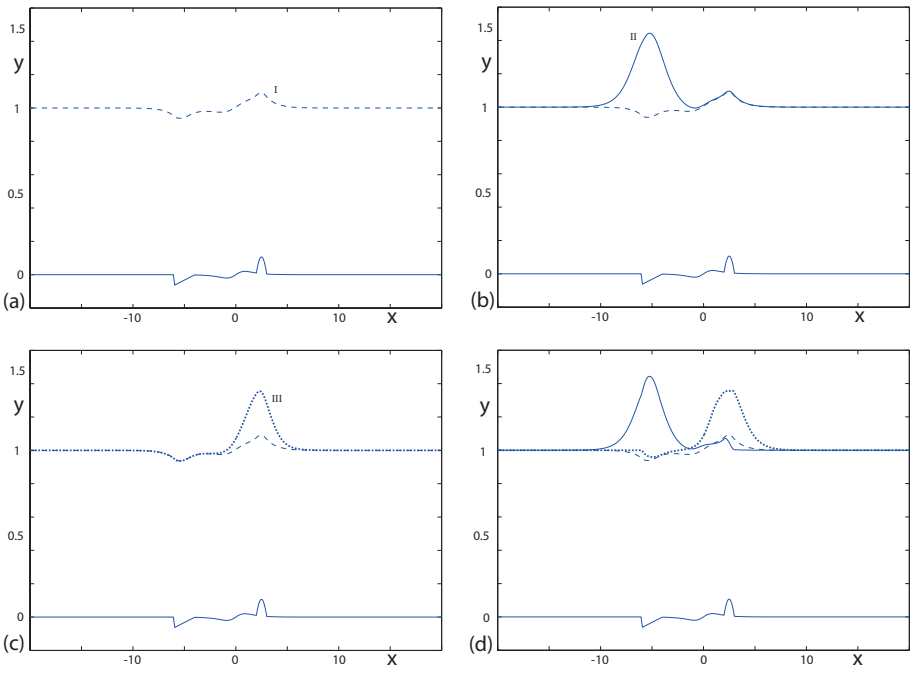

Figure 8: The free-surface waves corresponding to the bottom topography (20) with $\varepsilon = 0.04$ and $F = 1.2$: (a) hyperbolic solution (dashed curve), (b) first homoclinic solution computed using (14), (c) second homoclinic solution computerd using (14), and (d) both homoclinic solutions computed incorrectly by neglecting the tangential component η_t^{ε}.

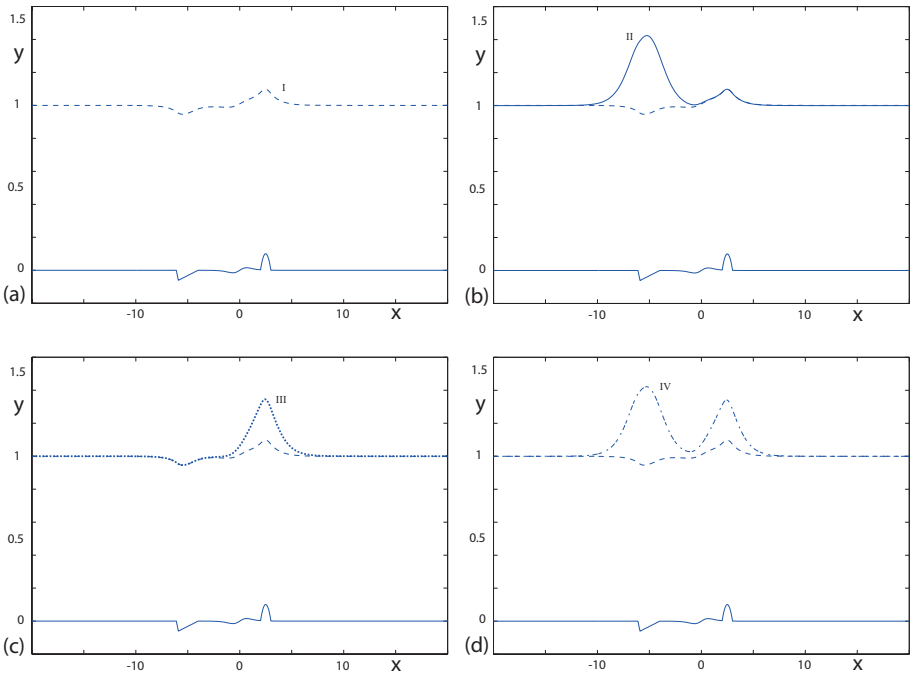

Figure 9: Numerically determined free-surface waves with bottom topography (20) with $\varepsilon = 0.04$ and $F = 1.2$: (a), (b) and (c) exactly correspond to the theoretical solutions of Fig. 8, while (d) shows the double-humped solitary wave IV, whose presence was suggested by waves II and III.

between the theoretical and numerical free-surface configurations is excellent. In Fig. 9(d), we show an additional solution we obtained numerically, inspired by our theoretical results of Fig. 8. Since the solitary wave II comes back down toward the hyperbolic trajectory around $x = -1$, while solitary wave III takes off from the hyperbolic trajectory at around the same x-value, we hypothesised the presence of a nearby wave which, having gone around the homoclinic manifold once in forming a wave close to II, then goes around it again to form a wave close to III. As an initial condition for numerical investigation of such a "double-looped" solitary wave we used the sum of theoretical waves II and III, and found the numerical solution IV as shown in Fig. 9(d). Thus, our theoretical method, in addition to giving explicit approximations, provides a method for making educated guesses at initial conditions for numerically discovering additional nonautonomous solitary waves.

As further examples illustrating the utility of our method, we show in Fig. 10 hyperbolic trajectories in several instances of sharp bottom topography. In all cases presented in Fig. 10, the *explicit* forms of the free surface expressions are given in Appendix C; nonsmooth p is no hindrance. For the particular case of Fig. 10(a) in which the bottom topography jumps from a height of 0 for $x < a$ to a height of ε for $x \geq a$, we can make an additional analytical observation.

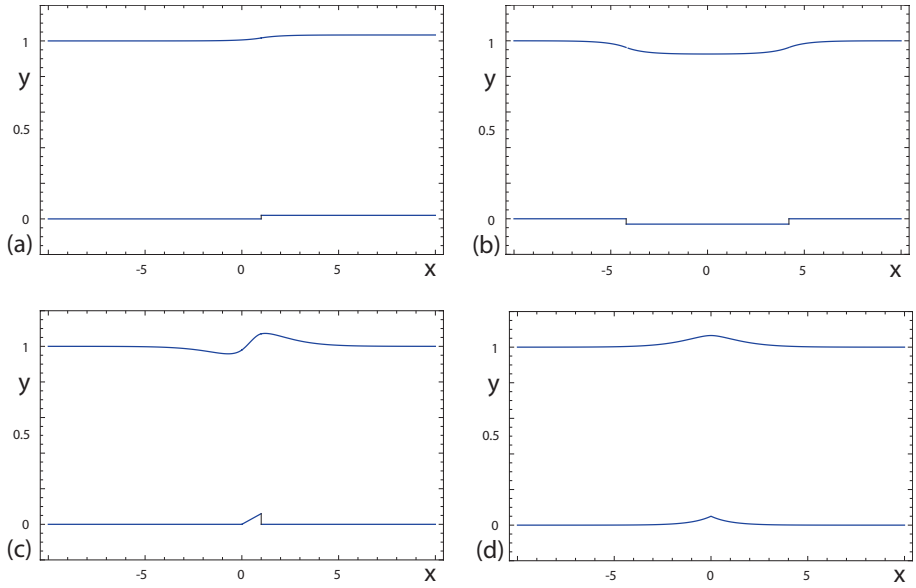

Figure 10: Explicitly obtained free surface configurations using (11) for a variety of specified bottom topographies, which are shown towards the bottom of each figure. (a) step using (C.3) with $F = 1.2$, $\varepsilon = 0.02$ and $F = 1.2$, (b) rectangular box using (C.5) with $F = 1.2$, $\varepsilon = -0.03$ and $a = 4.205$ (parameters used in Binder et al. [55]), (c) triangular wedge using (C.7) with $F = 1.2$, $\varepsilon = 0.03$, $a = 1$ and $b = 2$, (d) sharp exponentially decaying edge using (C.9) with $F = 1.2$, $\varepsilon = 0.05$ and $a = 1$.

Using (12) we compute

$$M(x) = \frac{\varepsilon}{\sqrt{6(F-1)}} \operatorname{sech}^2\left(\sqrt{\frac{3(F-1)}{2}}\,[a-x]\right)$$

which has no zero at any x value. The unstable manifold and the stable manifold of the hyperbolic trajectory (C.3) split apart such that they do not intersect. Thus, there is no near-solitary wave solution for this instance.

6. Concluding remarks

We have in this article used nonautonomous dynamical systems theory to address steady free-surface waves which result from arbitrary bottom topography. Our categorisation of hyperbolic and homoclinic solutions to the nonautonomous dynamical system correspond respectively to near-uniform and near-solitary wave solutions of the KdV equation. The advantages of our approach are the ability to obtain explicit formulæ, and the lack of necessity of conditions on p such as having compact support and being smooth. However, our method is perturbative, and depends on p being small. While this article required a

theoretical development in establishing the relevant formulæ, in a subsequent article we will perform an extensive numerical investigation of solutions, and indeed introduce several new types of solutions to the KdV equation prompted via our theoretical approach.

In computing the nonautonomous solitary wave (14), the $\mathcal{O}(\varepsilon)$-quantity $\eta_n^\varepsilon(x) + \eta_t^\varepsilon(x)$ will generically require numerical evaluation using the expressions (15) and (16) for a given forcing p. However, we do know that in the far field, the homoclinic solutions must approach the hyperbolic solution associated with it. Thus, $\eta_n^\varepsilon(x) + \eta_t^\varepsilon(x) \to \eta^\varepsilon(x)$ as $x \to \pm\infty$, and so we can think of

$$\begin{aligned}\eta_{\bar{x}}^\varepsilon(x) \quad &\approx \quad \bar{\eta}(x-\bar{x}) + \eta^\varepsilon(x) \approx 2\,(F-1)\,\mathrm{sech}^{\,2}\!\left(\sqrt{\frac{3(F-1)}{2}}[x-\bar{x}]\right) \\ &\quad + \frac{3}{2\sqrt{6(F-1)}} \int_0^\infty [p(x-\tau)+p(x+\tau)]\, e^{-\sqrt{6(F-1)}\tau}\mathrm{d}\tau\,. \end{aligned} \tag{21}$$

as being an *approximate* homoclinic solution whose integral—in contrast to those for η_n^ε and η_t^ε—is usually explicitly computable. It should be noted that the value(s) of $\bar{x}$ in using (21) must be first found by setting $M(x)$ in (12) to zero. In determining solitary waves numerically at higher accuracies, we therefore offer (21) as an excellent initial guess to choose for any numerical scheme.

As evidenced in the previous section, our method can also provide excellent guesses for the presence of multi-looped near-solitary waves. If M has n zero crossings, there will be n solitary-waves which are $\mathcal{O}(\varepsilon)$-close to solitary waves in the unperturbed problem. By choosing any linear combination of m of these, we can make a guess at an initial condition for a solitary wave which exhibits closeness to a linear combination of the unperturbed solitary waves. That is, the corresponding solutions will loop around the homoclinic manifold m times, each time shadowing a different unperturbed homoclinic trajectory. The potential total number of solitary waves we can get from this procedure is ${}^nC_1 + {}^nC_2 + \ldots + {}^nC_n = 2^n - 1$, by choosing $m = 1, 2, \cdots, n$. While we are not guaranteed to get exactly this number of solitary waves (since it is not clear whether each loop around the homoclinic will manage to exactly connect to another legitimate one), $2^n - 1$ provides an *estimate* for the total number of multi-looped nonautonomous solitary waves present in the system. Our theory has added impact since we can verify each of these possibilities by using a linear combination of our single-loop solitary waves as an educated initial guess in a numerical scheme.

Acknowledgements: SB acknowledges support from the Australian Research Council through Future Fellowship grant FT130100484.

Appendix A. Derivation of hyperbolic trajectory location (11)

In this section, we will outline how the formula (11) is derived, using recently developed techniques of nonautonomous dynamical systems. The principal theory used for this derivation is from Balasuriya [35]; related results also exist

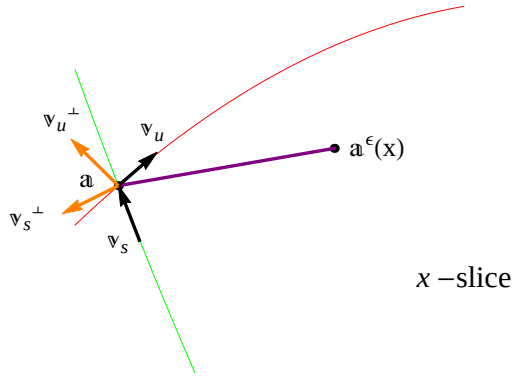

Figure A.11: The definitions of $\mathbf{v}_{s,u}$ and $\mathbf{v}_{s,u}^\perp$, and the shift in the hyperbolic trajectory $\mathbf{a}^\varepsilon(x) - \mathbf{a}$ (heavy line) in a general x-slice of the phase space of (A.2).

[36, 56]. We consider the general nonautonomous system

$$\dot{\mathbf{y}} = \mathbf{f}(\mathbf{y}) + \mathbf{g}(\mathbf{y}, x) \tag{A.1}$$

in which $\mathbf{y}$, $\mathbf{f}$ and $\mathbf{g}$ are two-dimensional, and the dot denotes the derivative with respect to the independent variable x. We assume that $\mathbf{g}$ is small, i.e., there exists a small ε such that $|\mathbf{g}(\mathbf{y}, x)| \leq \varepsilon$ for all $\mathbf{y} \in \mathbb{R}^2$ and $x \in \mathbb{R}$. When $\mathbf{g} \equiv \mathbf{0}$, (A.1) is autonomous since the vector field of the dynamical system does not depend on the independent variable x. We assume that in this situation (A.1) possesses a hyperbolic (saddle) fixed point $\mathbf{a}$. Thus $\mathbf{f}(\mathbf{a}) = \mathbf{0}$ since $\mathbf{a}$ is a fixed point, and the Jacobian derivative $D\mathbf{f}(\mathbf{a})$ possesses real eigenvalues λ_s and λ_u such that $\lambda_s < 0 < \lambda_u$. The fixed point $\mathbf{a}$ will possess a direction of attraction associated with the eigenvalue λ_s, which is characterised by the corresponding eigenvector $\mathbf{v}_s$ of $D\mathbf{f}(\mathbf{a})$. We will choose $\mathbf{v}_s$ to be a unit vector, and to point in the direction of flow, which in this case is inwards towards $\mathbf{a}$. Similarly, $\mathbf{a}$ possesses a direction of repulsion associated with the eigenvalue λ_u, with corresponding eigenvector $\mathbf{v}_u$ which we shall again choose to be normalised and point in the direction of flow. See Fig. A.11 for these quantities, which are associated with (A.1) when $\mathbf{g} \equiv \mathbf{0}$. The vectors $\mathbf{v}_s$ and $\mathbf{v}_u$ are tangential to respectively the stable and unstable manifolds of $\mathbf{a}$, which are each one-dimensional entities, and shown by the curves in Fig. A.11.

The system (A.1) could alternatively be viewed in terms of the augmented system

$$\left.\begin{array}{rcl} \dot{\mathbf{y}} & = & \mathbf{f}(\mathbf{y}) + \mathbf{g}(\mathbf{y}, t) \\ \dot{x} & = & 1 \end{array}\right\}. \tag{A.2}$$

The saddle point $\mathbf{a}$ that exists for (A.1) when $\mathbf{g} \equiv \mathbf{0}$ corresponds to a straight line trajectory $(\mathbf{a}, x)$ in the augmented system (A.2). This is a hyperbolic trajectory; it possesses stable and unstable manifolds which are each two-dimensional when viewed in relation to the augmented system (A.2). This situation is exactly that pictured in Fig. 2.

When $\mathbf{g} \neq \mathbf{0}$ but is small, the basic intuition is that this hyperbolic structure persists as a "wobbled" entity $(\mathbf{a}^\varepsilon(x), x)$, retaining its stable and unstable manifolds. The condition required on $\mathbf{g}$ for this persistence is that both $\mathbf{g}$ and $D\mathbf{g}$ are $\mathcal{O}(\varepsilon)$ for $(\mathbf{y}, x) \in \mathbb{R}^2 \times \mathbb{R}$ [35]. The technical difficulty in describing this persistence in the nonautonomous equation (A.1) is defining the intuitive structural characterisation of the perturbed trajectory as being a wobbled version of Fig. 2. The ideas of fixed points and eigenvalues are no longer applicable. Instead, the correct characterisation of the presence of both a stable and an unstable manifold is the concept of *exponential dichotomies* [42, 45, 46], which underscores two specialised directions in which exponential decay occurs in forwards and backwards x. The autonomous ($\mathbf{g} \equiv \mathbf{0}$) form of (A.1) possesses such an exponential dichotomy, with the rates of decay being precisely the eigenvalues $\lambda_{s,u}$. The fact that exponential dichotomies persist under perturbations (see Coppel [42]'s roughness theorem, also Yi [43], Yagasaki [44]) is what ensures that the hyperbolic trajectory persists when $\mathbf{g}$ is turned on in (A.1). We note that this hyperbolic trajectory is special in that it is the *only* trajectory which remains $\mathcal{O}(\varepsilon)$-close to the unperturbed hyperbolic trajectory $(\mathbf{a}, x)$ in *both* the limits $x \to \pm\infty$, since the wobbled geometry of Fig. 2 will ensure any other nearby trajectory will get pulled away in at least one of these limits. For example, if on one of the branches of the stable manifold, the trajectory will approach the hyperbolic trajectory in forwards x, but will go away from it in backwards x, thereby not remaining $\mathcal{O}(\varepsilon)$-close for all $x \in \mathbb{R}$. The same argument in reversed x is true if the trajectory is on one of the branches of the unstable manifold. If one takes any point which is on one of the other sheets lying in between stable and unstable manifold sheets, then its trajectory will in forwards x be pulled out in the direction of the unstable manifold, and in backwards x will be pulled out through the influence of the stable manifold. Thereby, any such trajectory can never remain $\mathcal{O}(\varepsilon)$-close for all x. Hence this nonautonomous viewpoint tells us that the hyperbolic trajectory $(\mathbf{a}^\varepsilon(x), x)$ is the *only* trajectory of the perturbed system (A.2) which remains $\mathcal{O}(\varepsilon)$-close to the unperturbed hyperbolic trajectory $(\mathbf{a}, x)$.

Recent work [35] enables characterising the location of the perturbed hyperbolic trajectory to leading-order. Let $\mathbf{v}_{s,u}^\perp$ be the corresponding normalised eigenvectors rotated by $+\pi/2$ in the anti-clockwise direction, and

$$\alpha_s(x) := -\int_0^\infty \mathbf{g}\left(\mathbf{a}, x+\tau\right) \cdot \mathbf{v}_s^\perp \, e^{-\lambda_u \tau} \, \mathrm{d}\tau \,, \tag{A.3}$$

$$\alpha_u(x) := \int_0^\infty \mathbf{g}\left(\mathbf{a}, x-\tau\right) \cdot \mathbf{v}_u^\perp \, e^{\lambda_s \tau} \, \mathrm{d}\tau \,. \tag{A.4}$$

If the perturbed hyperbolic trajectory is represented by $(\mathbf{a}_\varepsilon(x), x)$, Theorem 2.10 by Balasuriya [35] states that

$$\mathbf{a}_\varepsilon(x) - \mathbf{a} = \left[\alpha_u(x)\mathbf{v}_u^\perp - \frac{\alpha_u(x)\left(\mathbf{v}_s \cdot \mathbf{v}_u\right) - \alpha_s(x)}{\mathbf{v}_s \wedge \mathbf{v}_u}\mathbf{v}_u\right] \tag{A.5}$$

to leading-order in ε, where the wedge product for vectors $\mathbf{F} = (F_1, F_2)$ and

$\mathbf{G} = (G_1, G_2)$ in $\mathbb{R}^2$ is defined by

$$\mathbf{F} \wedge \mathbf{G} = F_1 G_2 - F_2 G_1 \,. \tag{A.6}$$

One way to think of (A.5) is to imagine taking a specific x-slice in the augmented phase space of (A.2). Then, $\mathbf{a}^\varepsilon(x) - \mathbf{a}$ represents the movement of the perturbed hyperbolic trajectory relative to the unperturbed one, as shown by the thick line in Fig. A.11. This quantity is represented in (A.5) in an orthogonal coordinate system comprising the unit vectors $\mathbf{v}_u$ and $\mathbf{v}_u^\perp$.

We now apply this general result to the KdV system (4). In correspondence with (A.1), we set

$$\mathbf{y}(x) := \begin{pmatrix} \eta(x) \\ \zeta(x) \end{pmatrix} \quad , \quad \mathbf{f} := \begin{pmatrix} \zeta \\ -\frac{9}{2}\eta^2 + 6(F-1)\eta \end{pmatrix} \quad \text{and} \quad \mathbf{g} := \begin{pmatrix} 0 \\ -3p(x) \end{pmatrix} .$$

The fixed point when $\mathbf{g} \equiv \mathbf{0}$ is $\mathbf{a} = (0, 0)$, and when examining the eigensystem of $D\mathbf{f}\,(\mathbf{a})$ we get

$$\lambda_s = -\sqrt{6(F-1)} \;,\; \mathbf{v}_s = \frac{1}{\sqrt{6F-5}} \begin{pmatrix} -1 \\ \sqrt{6(F-1)} \end{pmatrix}$$

and

$$\lambda_u = \sqrt{6(F-1)} \;,\; \mathbf{v}_u = \frac{1}{\sqrt{6F-5}} \begin{pmatrix} 1 \\ \sqrt{6(F-1)} \end{pmatrix} .$$

Thus

$$\mathbf{v}_s^\perp = \frac{1}{\sqrt{6F-5}} \begin{pmatrix} -\sqrt{6(F-1)} \\ 1 \end{pmatrix} \quad \text{and} \quad \mathbf{v}_u^\perp = \frac{1}{\sqrt{6F-5}} \begin{pmatrix} -\sqrt{6(F-1)} \\ 1 \end{pmatrix} .$$

Substituting into (A.3) and (A.4) gives

$$\alpha_s(x) = -\frac{3}{\sqrt{6F-5}} \int_0^\infty p(x+\tau) e^{-\sqrt{6(F-1)}\tau} \, \mathrm{d}\tau$$

and

$$\alpha_u(x) = -\frac{3}{\sqrt{6F-5}} \int_0^\infty p(x-\tau) e^{-\sqrt{6(F-1)}\tau} \, \mathrm{d}\tau \,.$$

We also have

$$\mathbf{v}_s \cdot \mathbf{v}_u = \frac{6F-7}{6F-5} \quad \text{and} \quad \mathbf{v}_s \wedge \mathbf{v}_u = \frac{2\sqrt{6(F-1)}}{6F-5} \,.$$

Now, since $\mathbf{a}_\varepsilon = (\eta^\varepsilon, \zeta^\varepsilon)$, it is only the first component of (A.5) that is of interest. Substituting everything into (A.5) and taking only the first component gives us (11), as desired. Additionally, we remark that the above argument on the fact that for the general system (A.2) $(\mathbf{a}^\varepsilon(x), x)$ is the *only* trajectory that remains within $\mathcal{O}(\varepsilon)$ of the unperturbed hyperbolic trajectory, ensures that for our system (4) the only free surface configuration that is uniformly $\mathcal{O}(\varepsilon)$-close to the flat free surface (i.e., the hyperbolic trajectory of the unperturbed system) is that given by $\eta^\varepsilon(x)$ in (11).

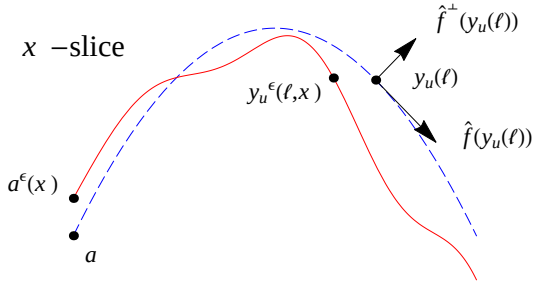

Figure B.12: The perturbed unstable manifold of (A.2) in an x-slice (solid curve) in relation to the unperturbed unstable manifold (dashed curve).

Appendix B. Derivation of homoclinic trajectory location (14)

Here, we outline the theoretical development of the homoclinic solutions (14), while establishing the condition (13) for a persistent homoclinic connection. We first describe the necessary theory, developed principally by Balasuriya [35] and extended to the present scenario, in the general setting of (A.1), which we repeat here:

$$\dot{\mathbf{y}} = \mathbf{f}(\mathbf{y}) + \mathbf{g}(\mathbf{y}, x) \ .$$

We first simplify the theory of Balasuriya [35] by setting $\operatorname{Tr} D\mathbf{f} = 0$, which is valid in our KdV context. Suppose $\mathbf{a}$ is a saddle fixed point of (A.1) with $\mathbf{g} \equiv \mathbf{0}$, which moreover has a homoclinic connection. This means that a branch of its one-dimensional unstable manifold coincides with a branch of its one-dimensional stable manifold, to form a trajectory which backwards and forwards asymptotes to $\mathbf{a}$. An example of this is exactly what is pictured as the heavy curve in Fig. 1, in which $\mathbf{a} = \mathbf{0}$ for this situation.

Now, if both $\mathbf{g}$ and $D\mathbf{g}$ remain $\mathcal{O}(\varepsilon)$, the theory of exponential dichotomies [42, 46, 43, 44] has already been quoted in Appendix A to argue that the saddle point perturbs to a nearby hyperbolic trajectory $(\mathbf{a}^{\varepsilon}(x), x)$ when (A.1) is expressed in the augmented form (A.2). The implication is that this hyperbolic trajectory locally retains both its stable and its unstable manifolds, which are *two-dimensional* entities in the augmented phase space (A.2). It is not necessary to have g be periodic in x [33, 47, 34, 48, cf.] for these manifolds to persist [37, 36, 35, 57]. However, unlike in the unperturbed system in which $\mathbf{g} \equiv \mathbf{0}$, there is no necessity for these manifolds to coincide.

Let us first focus on the unstable manifold. Suppose the unperturbed unstable manifold is expressible as $\mathbf{y}_u(x)$, in which $x \in [-\infty, P]$ for any finite P. In other words, $\mathbf{y}_u(x)$ is a solution to (A.1) with $\mathbf{g} \equiv \mathbf{0}$, such that $\mathbf{y}_u(x) \to \mathbf{a}$ as $x \to -\infty$, since $\mathbf{y}_u(x)$ is the unstable manifold of $\mathbf{a}$. As in Appendix A, we use the notation $\mathbf{F}^{\perp}$ to be the two-dimensional vector $\mathbf{F}$ rotated by $+\pi/2$ in the

anti-clockwise direction. Suppose moreover that a "hat" on a vector indicates that it has been normalised (divided by its length). With this in mind, we refer the reader to Fig. B.12, which shows a picture of the unstable manifold of (A.2) in a general x-slice. The dashed curve is the unperturbed unstable manifold $\mathbf{y}_u$, and we use ℓ as a parameter here to represent the location along the unstable manifold in this x-slice. At a particular location $\mathbf{y}_u(\ell)$ along this unperturbed unstable manifold, we have shown an orthonormal basis consisting of $\hat{\mathbf{f}}$ and $\hat{\mathbf{f}}^{\perp}$. The first of these is tangential to the unperturbed manifold since it represents the direction of flow when $\mathbf{g} \equiv \mathbf{0}$, while the second of these is normal to the unperturbed manifold.

The solid curve in Fig. B.12 is the intersection of the *perturbed* two-dimensional unstable manifold with the x-slice. This curve will be different in different x-slices, but we do know that the foot of this curve is at $\mathbf{a}^{\varepsilon}(x)$, since this is the location of the hyperbolic trajectory to which the unstable manifold is attached. Now, there is a point $(\mathbf{y}_u^{\varepsilon}(\ell, x), x)$ on this manifold which is $\mathcal{O}(\varepsilon)$-close to the point $\mathbf{y}_u(\ell)$, such that this closeness persists when both points are iterated backwards in x. The location of $\mathbf{y}_u^{\varepsilon}(\ell, x)$ as ℓ and x therefore characterises the location of the two-dimensional unstable manifold in the augmented system. Theorems 2.1 and 2.3 by Balasuriya [35] (see also Remark 2.6) quantify this precisely by

$$\mathbf{y}_u^{\varepsilon}(\ell, x) = \mathbf{y}_u(\ell) + \left[\frac{M^u(\ell, x)}{|\mathbf{f}(\mathbf{y}_u(\ell))|} \hat{\mathbf{f}}^{\perp}(\mathbf{y}_u(\ell)) + \frac{B^u(\ell, x)}{|\mathbf{f}(\mathbf{y}_u(\ell))|} \hat{\mathbf{f}}(\mathbf{y}_u(\ell)) \right] + \mathcal{O}(\varepsilon^2) \quad \text{(B.1)}$$

for $\ell \in [-\infty, P]$ and $x \in [-\infty, Q]$ for any finite P, Q, with

$$M^u(\ell, x) := \int_{-\infty}^{\ell} \mathbf{f}(\mathbf{y}_u(\tau)) \wedge \mathbf{g}(\mathbf{y}_u(\tau), \tau + x - \ell) \, \mathrm{d}\tau \quad \text{(B.2)}$$

and

$$B^u(\ell, x) := |\mathbf{f}(\mathbf{y}_u(\ell))|^2 \int_0^{\ell} \frac{\Omega^u(\tau) M^u(\ell, \tau + x - \ell) + \mathbf{f}(\mathbf{y}_u(\tau)) \cdot \mathbf{g}(\mathbf{y}_u(\tau), \tau + x - \ell)}{|\mathbf{f}(\mathbf{y}_u(\tau))|^2} \mathrm{d}\tau \quad \text{(B.3)}$$

in which

$$\Omega^u(\tau) := \hat{\mathbf{f}}^T(\mathbf{y}_u(\tau)) \left[(D\mathbf{f})^T(\mathbf{y}_u(\tau)) + D\mathbf{f}(\mathbf{y}_u(\tau)) \right] \hat{\mathbf{f}}^{\perp}(\mathbf{y}_u(\tau)) \quad \text{(B.4)}$$

and the wedge product is defined in (A.6). The quantity M^u is associated with a "normal" movement to the original unperturbed manifold, while B^u is a "tangential" movement whose existence and importance was first presented by Balasuriya [35], and developed further [36, 58].

Now let us turn to characterising the stable manifold. Suppose that $\mathbf{y}_s(x)$ represents the stable manifold solution to (A.1) with $\mathbf{g} \equiv \mathbf{0}$. Using exactly the same sorts of description as for the unstable manifold, Theorems 2.7 and 2.8 (see also Remark 2.9) by Balasuriya [35] quantifies exactly this. It is shown that this two-dimensional surface is parametrically representible by

$$\mathbf{y}_s^{\varepsilon}(\ell, x) = \mathbf{y}_s(\ell) + \left[\frac{M^s(\ell, x)}{|\mathbf{f}(\mathbf{y}_s(\ell))|} \hat{\mathbf{f}}^{\perp}(\mathbf{y}_s(\ell)) + \frac{B^s(\ell, x)}{|\mathbf{f}(\mathbf{y}_s(\ell))|} \hat{\mathbf{f}}(\mathbf{y}_s(\ell)) \right] + \mathcal{O}(\varepsilon^2) \quad \text{(B.5)}$$

for $\ell \in [P, \infty]$ and $x \in [Q.\infty]$ for any finite P, Q, with

$$M^s(\ell, x) := -\int_\ell^\infty \mathbf{f}\left(\mathbf{y}_s(\tau)\right) \wedge \mathbf{g}\left(\mathbf{y}_s(\tau), \tau + x - \ell\right) \, \mathrm{d}\tau \tag{B.6}$$

and

$$B^s(\ell, x) := \left|\mathbf{f}\left(\mathbf{y}_s(\ell)\right)\right|^2 \int_0^\ell \frac{\Omega^s(\tau) M^s(\ell, \tau + x - \ell) + \mathbf{f}\left(\mathbf{y}_s(\tau)\right) \cdot \mathbf{g}\left(\mathbf{y}_s(\tau), \tau + x - \ell\right)}{\left|\mathbf{f}\left(\mathbf{y}_s(\tau)\right)\right|^2} \mathrm{d}\tau \tag{B.7}$$

in which

$$\Omega^s(\tau) := \hat{\mathbf{f}}^T\left(\mathbf{y}_s(\tau)\right) \left[\left(D\mathbf{f}\right)^T \left(\mathbf{y}_s(\tau)\right) + D\mathbf{f}\left(\mathbf{y}_s(\tau)\right) \right] \hat{\mathbf{f}}^\perp\left(\mathbf{y}_s(\tau)\right) . \tag{B.8}$$

Now in our problem, we have an unperturbed *homoclinic* trajectory, and thus $\mathbf{y}_u = \mathbf{y}_s$. We will set $\mathbf{y}_\sigma$ to be either of these, and thus $\mathbf{y}_\sigma(x)$ is the unperturbed homoclinic trajectory of (A.1) when $\mathbf{g} \equiv \mathbf{0}$. (There is a subtle difference between $\mathbf{y}_u$ and $\mathbf{y}_s$ in this homoclinic case: $\mathbf{y}_u(x)$ is defined for $[-\infty, P]$ for any finite P, while $\mathbf{y}_s(\ell)$'s domain of definition is of the form $[P, \infty]$. This will be accounted for in what follows.) Suppose ℓ is fixed, and consider a normal line drawn at $\mathbf{y}_\sigma(\ell)$ in an x-slice. So if we have a nearby homoclinic point, we need $\mathbf{y}_s^\varepsilon(\ell, x) = \mathbf{y}_u^\varepsilon(\ell, x)$ in (B.1) and (B.5). Now, for an intersection between the stable and unstable manifolds to occur on this normal vector, we need $M^u(\ell, x)$ in (B.2) and $M^s(\ell, x)$ in (B.6) to be identical, which leads to the necessary condition for an intersection:

$$\tilde{M}(\ell, x) := \int_{-\infty}^\infty \mathbf{f}\left(\mathbf{y}_\sigma(\tau)\right) \wedge \mathbf{g}\left(\mathbf{y}_\sigma(\tau), \tau + x - \ell\right) \, \mathrm{d}\tau = 0 . \tag{B.9}$$

The above condition (B.9) by itself is not a sufficient condition for an intersection between the stable and unstable manifolds, since there are $\mathcal{O}(\varepsilon^2)$-corrections in (B.1) and (B.5). On the other hand, if it is true that $\tilde{M}$ as a function of x crosses zero at a specific x value (let us call it $\bar{x}$), then such a crossing is structurally stable. That is, under small perturbations this zero-crossing persists, and therefore a homoclinic connection exists in a x-slice within $\mathcal{O}(\varepsilon)$ of $\bar{x}$. If $\tilde{M}$ is differentiable in x, a similar characterisation could be presented more formally using the implicit function theorem to say that if there exists $\bar{x}$ such that $\tilde{M}(\ell, \bar{x}) = 0$ and $\tilde{M}_x(\ell, \bar{x}) \neq 0$ (in which the subscript x represents the x-derivative), then there is a nearby homoclinic connection (this is a standard Melnikov function approach; see Guckenheimer and Holmes [33], Wiggins [34]).

In translating these general results to the KdV problem, we set

$$\mathbf{y}(x) = \begin{pmatrix} \eta(x) \\ \zeta(x) \end{pmatrix} \quad , \quad \mathbf{f} = \begin{pmatrix} \zeta \\ -\frac{9}{2}\eta^2 + 6(F-1)\eta \end{pmatrix} \quad \text{and} \quad \mathbf{g} = \begin{pmatrix} 0 \\ -3p(x) \end{pmatrix} .$$

The unperturbed homoclinic trajectory $\mathbf{y}_\sigma(\tau)$ can be represented by

$$\mathbf{y}_\sigma(\tau) = \begin{pmatrix} \bar{\eta}(\tau) \\ \bar{\eta}'(\tau) \end{pmatrix}$$

in terms of the fundamental solitary wave solution (8). Therefore,

$$\mathbf{f}\left(\mathbf{y}_\sigma(\tau)\right) \wedge \mathbf{g}\left(\mathbf{y}_\sigma(\tau), \tau + x - \ell\right)) = -3p(\tau - x - \ell)\bar{\eta}'(\tau) \tag{B.10}$$

and thus from (B.9) for an intersection in the slice $\bar{x}$ along a normal drawn at $\mathbf{y}_\sigma(\ell)$ we need

$$\int_{-\infty}^{\infty} \bar{\eta}'(\tau) p(\tau + \bar{x} - \ell)\, \mathrm{d}\tau = 0\,.$$

We choose to draw our normal at $\ell = 0$. This corresponds to the symmetric point at which $\bar{\eta} = 2(F-1)$ and $\bar{\eta}' = 0$ as shown in Fig. 4, and thus our choice of normal is exactly N as in Fig. 4. Thus, our condition above becomes

$$\int_{-\infty}^{\infty} \bar{\eta}'(\tau) p(\tau + \bar{x})\, \mathrm{d}\tau = 0$$

for the presence of an intersection between the stable and unstable manifolds in a x-slice $\bar{x}$ along N. Inserting $\bar{\eta}$ as given in (7) leads to

$$\int_{-\infty}^{\infty} \operatorname{sech}^2\left(\sqrt{\frac{3(F-1)}{2}}\tau\right) \tanh\left(\sqrt{\frac{3(F-1)}{2}}\tau\right) p(\tau + \bar{x})\, \mathrm{d}\tau = 0\,,$$

and thus we have derived (12) and (13). So any $\bar{x}$ which satisfies the above such that $M(\bar{x})$ crosses zero at $\bar{x}$ corresponds to an intersection of the stable and unstable manifold, and thus a homoclinic connection. On the other hand, if there is no $\bar{x}$ which satisfies this condition, then for small enough ε there will not be an intersection of the stable and unstable manifolds, and so a homoclinic connection will not persist.

Assuming a homoclinic connection exists, we next determine the free surface $\eta^\varepsilon_{\bar{x}}(x)$ which corresponds to this value of $\bar{x}$. We have already determined that in the x-slice $\bar{x}$, there is an intersection between the stable and unstable manifolds. This intersection, when evolved in backwards x, lies on the unstable manifold. Also, this intersection, when evolved in forwards x, lies on the stable manifold. We will determine the entire x-evolution (for all $x \in \mathbb{R}$) by "stitching together" the backwards x evolution (using the unstable manifold expression (B.1) for $x \in [-\infty, \bar{x}]$), with the forwards x evolution (using the stable manifold expression (B.5) for $x \in [\bar{x}, \infty]$). We note though that (B.1) and (B.5) give the two-dimensional position of the homoclinic in terms of the coordinates (η, ζ), and thus we can limit our attention to the first component of each of these expressions.

Now, in the x-slice $\bar{x}$, our homoclinic is at the location $\mathbf{y}^\varepsilon_u(0, \bar{x})$, or equivalently $\mathbf{y}^\varepsilon_s(0, \bar{x})$, since we chose $\ell = 0$. As x evolves, this homoclinic will stay close to the unperturbed homoclinic trajectory $\mathbf{y}_\sigma(x - \bar{x})$, since this is the specific unperturbed homoclinic trajectory which is shadowed by the perturbed one, and in particular is near $\mathbf{y}_\sigma(0)$ when $x = \bar{x}$. Thus, in a general x-slice, we need to locate the perturbed homoclinic trajectory along a normal drawn

at $\mathbf{y}_\sigma(x-\bar{x})$; this is illustrated in Fig. 5 as N_x. Therefore, we will recover the perturbed homoclinic by

$$\eta_{\bar{x}}^{\varepsilon}(x) = \begin{cases} \mathbf{y}_u^{\varepsilon}\left(x-\bar{x},x\right)\Big|_1 & \text{if } x \le \bar{x} \\ \mathbf{y}_s^{\varepsilon}\left(x-\bar{x},x\right)\Big|_1 & \text{if } x > \bar{x} \end{cases} \tag{B.11}$$

in which the subscript 1 stands for the first component of the vector.

Before we apply (B.1) and (B.5) to evaluate (B.11), we shall write $\mathbf{f}$ slightly differently for convenience. Since $\zeta = \eta'$, and since the second component of $\mathbf{f}$ is alternatively expressed from (4) as $\zeta' = \eta''$, we will write

$$\mathbf{f}\left(\mathbf{y}_\sigma\right) = \begin{pmatrix} \bar{\eta}' \\ \bar{\eta}'' \end{pmatrix}$$

and so, when evaluated at $\mathbf{y}_\sigma$,

$$|\mathbf{f}| = \sqrt{\left(\bar{\eta}'\right)^2 + \left(\bar{\eta}''\right)^2},\ \hat{\mathbf{f}} = \frac{1}{\sqrt{\left(\bar{\eta}'\right)^2 + \left(\bar{\eta}''\right)^2}} \begin{pmatrix} \bar{\eta}' \\ \bar{\eta}'' \end{pmatrix},\ \hat{\mathbf{f}}^{\perp} = \frac{1}{\sqrt{\left(\bar{\eta}'\right)^2 + \left(\bar{\eta}''\right)^2}} \begin{pmatrix} -\bar{\eta}'' \\ \bar{\eta}' \end{pmatrix}.$$

Thus we can write

$$\left.\frac{\hat{\mathbf{f}}^{\perp}}{|\mathbf{f}|}\right|_1 = \frac{-\bar{\eta}''}{\left(\bar{\eta}'\right)^2 + \left(\bar{\eta}''\right)^2} \quad \text{and} \quad \left.\frac{\hat{\mathbf{f}}}{|\mathbf{f}|}\right|_1 = \frac{\bar{\eta}'}{\left(\bar{\eta}'\right)^2 + \left(\bar{\eta}''\right)^2}.$$

Moreover, Ω^u and Ω^s are identical since $\mathbf{y}_u$ and $\mathbf{y}_s$ are the same, and we can redefine these to be called Ω. Substituting the formulæ for $\mathbf{f}$ into (B.4) or (B.8) and simplifying leads to the expression (17). Now, since we have already calculated $\mathbf{f} \wedge \mathbf{g}$ in (B.10), we may insert this into (B.2) to get

$$M^u(\ell, x) = -3\int_{-\infty}^{\ell} \bar{\eta}'(\tau) p\left(\tau + x - \ell\right)\, \mathrm{d}\tau\,.$$

Therefore,

$$M^u(x-\bar{x}, x) = -3\int_{-\infty}^{x-\bar{x}} \bar{\eta}'(\tau) p\left(\tau + \bar{x}\right)\, \mathrm{d}\tau\,,$$

and we now have all the elements to determine the normal component for $x \le \bar{x}$. To compute the tangential component, we note that

$$\mathbf{f} \cdot \mathbf{g} = -3\bar{\eta}'' p$$

and thus from (B.3),

$$\begin{aligned} B^u(x-\bar{x},x) &= |\mathbf{f}\left(\mathbf{y}_u(x-\bar{x})\right)|^2 \int_0^{x-\bar{x}} \frac{\Omega(\tau) M^u(x-\bar{x},\tau+\bar{x}) + \mathbf{f}\left(\mathbf{y}_u(\tau)\right)\cdot\mathbf{g}\left(\mathbf{y}_u(\tau),\tau+\bar{x}\right)}{\left|\mathbf{f}\left(\mathbf{y}_u(\tau)\right)\right|^2}\mathrm{d}\tau \\ &= \left[\bar{\eta}'(x-\bar{x})^2 + \bar{\eta}''(x-\bar{x})^2\right] \\ &\times \int_0^{x-\bar{x}} \frac{-3\Omega(\tau)\int_{-\infty}^{x-\bar{x}} \bar{\eta}'(\lambda) p(\lambda + [\tau+\bar{x}] - [x-\bar{x}])\mathrm{d}\lambda + [-3p(\tau+\bar{x})\bar{\eta}''(\tau)]}{\bar{\eta}'(\tau)^2 + \bar{\eta}''(\tau)^2}\mathrm{d}\tau \end{aligned}$$

We now have all the terms to compute the $x \leq \bar{x}$ term in (B.11). The term arising from M^u gives the normal component, which has been included in the expression for η_n^ε in (15). The term arising from B^u gives the tangential component, which has been incorporated into the expression for η_t^ε in (16).

Next, essentially the same calculation can be done for M^s and B^s, in order to determine the expressions for $x > \bar{x}$ as given in (15) and (16). These are omitted for brevity.

Appendix C. Explicit formulæ for perturbations of a uniform stream

This appendix outlines some explicit formulæ for the free surface due to various forms of p; it is the basis for the preparation of Fig. 10. Since the combination of terms $\sqrt{6(F-1)}$ occurs frequently in all the formulæ here, we use the shorthand notation

$$\gamma := \sqrt{6(F-1)}\,. \tag{C.1}$$

Appendix C.1. Step

The easiest nonzero topography to deal with is that of a step given by

$$p(x) = \begin{cases} 0 & \text{if } x < a \\ \varepsilon & \text{if } x \geq a \end{cases}, \tag{C.2}$$

for some parameter a at which the step is located. By choosing ε either positive or negative, the step could be either a step up or a step down when proceeding from left to right. Now, utilising (11) gives us the result

$$\eta^\varepsilon(x) \approx \begin{cases} \dfrac{\varepsilon}{6(F-1)} e^{\gamma(x-a)} & \text{if } x < a \\ \dfrac{\varepsilon}{6(F-1)} \left[2 - e^{\gamma(a-x)}\right] & \text{if } x \geq a \end{cases}, \tag{C.3}$$

with error $\mathcal{O}(\varepsilon^2)$. This goes to zero as $x \to -\infty$, and to $\varepsilon/(3(F-1))$ as $x \to \infty$, consistent with the prediction that if $p(x) = \varepsilon$ (a constant), the fixed point at $\eta = 0$ moves to this new location.

Appendix C.2. Rectangular bump

Consider a rectangular bump/depression of width $2a$ given by

$$p(x) = \begin{cases} \varepsilon & \text{if } |x| < a \\ 0 & \text{if } |x| > a \end{cases}, \tag{C.4}$$

where $\varepsilon > 0$ constitutes a raised rectangular bump, and $\varepsilon < 0$ a rectangular depression. Performing calculations using (11) gives

$$\eta^\varepsilon(x) \approx \begin{cases} \dfrac{\varepsilon}{2(F-1)} \left[1 - e^{-a\gamma} \cosh(\gamma x)\right] & \text{if } |x| \leq a \\ \dfrac{\varepsilon}{2(F-1)} \sinh(a\gamma)\, e^{-\gamma|x|} & \text{if } |x| > a \end{cases} \tag{C.5}$$

with error $\mathcal{O}(\varepsilon^2)$. This solution is differentiable at $x = \pm a$, despite p's jump discontinuities at these values.

Appendix C.3. Triangular wedge

Consider a triangular wedge located in the region $x \in [0, a]$, with height changing linearly from 0 at $x = 0$ to b at $x = a$. Thus

$$p(x) = \begin{cases} \varepsilon \frac{b}{a} x & \text{if } 0 \le x < a \\ 0 & \text{if } x < 0 \text{ or } x > a \end{cases} , \tag{C.6}$$

where positive ε corresponds to a triangular wedge sticking up into the channel, while negative ε would be a triangular depression. Performing calculations using (11) gives the explicit formula

$$\frac{4\gamma a(F-1)\eta^{\varepsilon}(x)}{\varepsilon b} \approx \begin{cases} e^{\gamma x}\left[e^{-\gamma a}\left(1+\gamma(a-2x)\right)+2\gamma x-1\right] & \text{if } x \le 0 \\ 2\gamma x - e^{-\gamma x}\left(1+2\gamma x\right) + e^{\gamma(x-a)}\left(1+\gamma(a-2x)\right) & \text{if } 0 < x \le a \\ e^{-\gamma x}\left[e^{\gamma a}\left(1+\gamma(2x-a)\right)-2\gamma x-1\right] & \text{if } x > a \end{cases} \tag{C.7}$$

Appendix C.4. Sharp edge/pit

Now consider

$$p(x) = \varepsilon e^{-a|x|} \tag{C.8}$$

for $a > 0$, which is a sharp edge at $x = 0$, but with the topography easing to zero as $x \to \pm\infty$. If $\varepsilon < 0$, this is a pit at $x = 0$, while if $\varepsilon > 0$, it is an edge jutting up. In either case (11) gives the result

$$\eta^{\varepsilon}(x) \approx \begin{cases} \dfrac{3\varepsilon}{[a^2-\gamma^2]\,\gamma}\left[a e^{-\gamma|x|} - \gamma e^{-a|x|}\right] & \text{if } a \ne \sqrt{6(F-1)} \\ \dfrac{\varepsilon}{4(F-1)} e^{-\gamma|x|}\left(1+\gamma\,|x|\right) & \text{if } a = \sqrt{6(F-1)} \end{cases} . \tag{C.9}$$

It is instructive that the decay at $\pm\infty$ is at a rate which involves both the scale factor a of the bottom topography and the quantity $\gamma = \sqrt{6(F-1)}$ which incorporates the Froude number. The surface's decay at $\pm\infty$ occurs exponentially, at a rate no quicker than the smaller of these coefficients. When these are identical, the decay rate is (slightly) slower than exponential, as given in the second equation above, but to all intents and purposes does not look very different.

[1] D. J. Korteweg, G. de Vries, On the change of form of long waves advancing in a rectangular canal, and on a new type of long stationary waves, Phil. Mag. 5 (1895) 422.

[2] N. J. Zabusky, M. D. Kruskal, Interaction of "solitons" in a collision less plasma and the recurrence of initial states, Phys. Rev. Lett. 15 (1965) 240–243.

[3] J. W. Miles, The Korteweg-de Vries equation: a historical essay, J. Fluid Mech. 106 (1984) 131–147.

[4] T. R. Akylas, On the excitation of long nonlinear water waves by a moving pressure distribution, J. Fluid Mech. 141 (1984) 455.

[5] S. S.-P. Shen, On the accuracy of the stationary forced Korteweg-de Vries equation as a model equation for flows over a bump, Q. J. Appl. Math. 53 (1995) 701.

[6] E. Fermi, J. Pasta, S. Ulam, Studies of nonlinear problems, Nonlinear Wave motion. Lectures in Applied Mathematics 15 (1955) 143–156.

[7] M. Erdogan, N. Tzirakis, V. Zharnitsky, Nearly linear dynamics of nonlinear dispersive waves, Phys. D 240 (2011) 1325–1333.

[8] T. Grava, C. Klein, A numerical study of the small dispersion limit of the Korteweg–de Vries equation and asymptotic solutions, Phys. D 241 (2012) 2246–2264.

[9] T. Trogdon, S. Olver, B. Deconinck, Numerical inverse scattering for the Korteweg–de Vries and modified Korteweg–de Vries equations, Phys. D 241 (2012) 1003–1025.

[10] T. Trogdon, B. Deconinck, A Riemann–Hilbert problem for the finite-genus solutions of the KdV equation and its numerical solution, Phys. D 251 (2013) 1–18.

[11] F. Chardard, F. Dias, H. Nguyen, J.-M. Vanden-Broeck, Stability of some stationary solutions to the forced KdV equation with one or two bumps, J. Engng. Math 70 (2011) 175.

[12] R. Grimshaw, M. Maleewong, Stability of steady gravity waves generated by a moving localised pressure disturbance in water of finite depth, Phys. Fluids 25 (2013) 076605.

[13] H. Kim, H. Park, D. Yoon, Numerical stability analysis of steady solutions for the forced kdv equation based on the polynomial chaos expansion, Eur. J. Mech. B Fluids 39 (2013) 71–86.

[14] S. Cole, Transient waves produced by flow past a bump, Wave Motion 7 (1985) 579–587.

[15] R. Grimshaw, N. Smyth, Resonant flow of a stratified fluid over topography, J. Fluid Mech. 169 (1986) 429–464.

[16] B. J. Binder, J.-M. Vanden-Broeck, F. Dias, Forced solitary waves and fronts past submerged obstacles, Chaos 15 (2005) 037106.

[17] B. J. Binder, M. G. Blyth, Electrified free-surface flow of an inviscid liquid past topography, Phys. Fluids. 24 (2012) 102112.

[18] J. Choi, S. Sun, S. Whang, Supercritical surface gravity waves generated by a positive forcing, Eur. J. Mech. B Fluids 27 (2008) 750–770.

[19] A. Jeffrey, T. Kakutani, Weak nonlinear dispersive waves: a discussion centered around the Korteweg-de Vries equation, SIAM Rev. 14 (1972) 582–643.

[20] F. Dias, J.-M. Vanden-Broeck, Generalised critical free-surface flows, J. Eng. Math. 42 (2002) 291.

[21] B. J. Binder, J.-M. Vanden-Broeck, Free-surface flow past surfboards and sluice gates, Eur. J. Appl. Math. 16 (2005) 601–619.

[22] B. J. Binder, F. Dias, J.-M. Vanden-Broeck, Steady free-surface flow past an uneven channel bottom, Theor. Comput. Fluid Dyn. 20 (2006) 124.

[23] B. K. Ee, R. Grimshaw, D.-H. Zhang, K. W. Chow, Steady transcritical flow over a hole: Parametric map of solutions of the forced Korteweg–de Vries equation, Phys. Fluids 22 (2010) 056602.

[24] B. J. Binder, J.-M. Vanden-Broeck, The effect of disturbances on the flows under a sluice gate and past an inclined plate, J. Fluid Mech. 576 (2007) 475.

[25] B. J. Binder, J.-M. Vanden-Broeck, Hybrid free-surface flows in a two dimensional channel, Phys. Rev. E 84 (2011) 016302.

[26] R. Grimshaw, Transcritical flow past an obstacle, ANZIAM J. 52 (2011) 1.

[27] R. Grimshaw, X. Tian, Periodic and chaotic behaviour in a reduction of the perturbed Korteweg-de Vries equation, Proc. R. Soc. Lond. A 445 (1994) 1–21.

[28] K. Blyuss, Chaotic behaviour of solutions to a perturbed Korteweg-de Vries equation, Reports Math. Phys. 49 (2002) 29–38.

[29] N. Zhang, G. Yang, Solitary waves and chaos in nonlinear visco-elastic rod, Eur. J. Mech. 22 (2003) 917–923.

[30] J. Roessler, Application of Melnikov's method to the reduced KdV equation, Aust. J. Phys. 44 (1991) 15–32.

[31] B. Birnir, Chaotic perturbations of KdV, Phys. D 19 (1986) 238–254.

[32] V. K. Melnikov, On the stability of the centre for time-periodic perturbations, Trans. Moscow Math. Soc. 12 (1963) 1–56.

[33] J. Guckenheimer, P. Holmes, Nonlinear Oscillations, Dynamical Systems and Bifurcations of Vector Fields, Springer, New York, 1983.

[34] S. Wiggins, Chaotic Transport in Dynamical Systems, Springer-Verlag, New York, 1992.

[35] S. Balasuriya, A tangential displacement theory for locating perturbed saddles and their manifolds, SIAM J. Appl. Dyn. Sys. 10 (2011) 1100–1126.

[36] S. Balasuriya, Nonautonomous flows as open dynamical systems: characterising escape rates and time-varying boundaries, in: W. Bahsoun, C. Bose, G. Froyland (Eds.), Ergodic Theory, Open Dynamics and Coherent Structures, Springer, 2014, pp. 1–30.

[37] S. Balasuriya, Cross-separatrix flux in time-aperiodic and time-impulsive flows, Nonlinearity 19 (2006) 282–311.

[38] J. M. Vanden-Broeck, Free-surface flow over an obstruction in a channel, Phys. Fluids 30 (1987) 2315.

[39] B. Binder, M. Blythe, S. Balasuriya, Non-uniqueness of steady free-surface flow at critical Froude number, Europhys. Lett. 105 (2014) 44003.

[40] K. Blyuss, Chaotic behaviour of nonlinear waves and solutions of perturbed Korteweg-de Vries equation, Reports Math. Phys. 46 (2000) 47–54.

[41] J. Choi, T. Lin, S. Sun, S. Whang, Supercritical surface waves generated by negative or oscillatory forcing, Discrete Cont. Dyn. Sys. B 14 (2010) 1313–1335.

[42] W. Coppel, Dichotomies in Stability Theory, number 629 in Lecture Notes in Mathematics, Springer-Verlag, Berlin, 1978.

[43] Y. Yi, A generalized integral manifold theorem, J. Differential Equations 102 (1993) 153–187.

[44] K. Yagasaki, Invariant manifolds and control of hyperbolic trajectories on infinite- or finite-time intervals, Dyn. Sys. 23 (2008) 309–331.

[45] R. Sacker, G. Sell, Existence of dichotomies and invariant splitting for linear differential systems: I, J. Diff. Equations 15 (1974) 429–458.

[46] K. Palmer, Exponential dichotomies and transversal homoclinic points, J. Diff. Equations 55 (1984) 225–256.

[47] V. Rom-Kedar, A. Leonard, S. Wiggins, An analytical study of transport, mixing and chaos in an unsteady vortical flow, J. Fluid Mech. 214 (1990) 347–394.

[48] S. Balasuriya, Direct chaotic flux quantification in perturbed planar flows: general time-periodicity, SIAM J. Appl. Dyn. Sys. 4 (2005) 282–311.

[49] S. Balasuriya, Optimal perturbation for enhanced chaotic transport, Phys. D 202 (2005) 155–176.

[50] S. Balasuriya, Approach for maximizing chaotic mixing in microfluidic devices, Phys. Fluids 17 (2005) 118103.

[51] S. Balasuriya, M. Finn, Energy constrained transport maximization across a fluid interface, Phys. Rev. Lett. 108 (2012) 244503.

[52] S. Balasuriya, Optimal frequency for microfluidic mixing across a fluid interface, Phys. Rev. Lett. 105 (2010) 064501.

[53] V. Hur, Exact solitary water waves with vorticity, Arch. Rat. Mech. Anal. 188 (2008) 213–244.

[54] S. Wade, B. Binder, T. Mattner, J. Denier, On the free-surface flow of very steep forced solitary waves, J. Fluid Mech. 739 (2014) 1–29.

[55] B. Binder, F. Dias, J.-M. Vanden-Broeck, Influence of rapid changes in a channel bottom on free-surface flows, IMA J. Appl. Math. 73 (2008) 254–273.

[56] S. Balasuriya, K. Padberg-Gehle, Controlling the unsteady analogue of saddle stagnation points, SIAM J. Appl. Math. 73 (2013) 1038–1057.

[57] S. Balasuriya, Explicit invariant manifolds and specialised trajectories in a class of unsteady flows, Phys. Fluids 24 (2012) 127101.

[58] S. Balasuriya, K. Padberg-Gehle, Nonautonomous control of stable and unstable manifolds in two-dimensional flows, Phys. D 276 (2014) 48–60.